



Universiteit
Leiden
The Netherlands

Discovery of Three $z > 6.5$ Quasars in the VISTA Kilo-Degree Infrared Galaxy (VIKING) Survey

Venemans, B.; Findlay, J.; Sutherland, W.; De Rosa, G.; McMahon, R.; Simcoe, R.; ... ; De, Rosa G.

Citation

Venemans, B., Findlay, J., Sutherland, W., De Rosa, G., McMahon, R., Simcoe, R., ... Lewis, J. (2013). Discovery of Three $z > 6.5$ Quasars in the VISTA Kilo-Degree Infrared Galaxy (VIKING) Survey. *The Astrophysical Journal*, 779, 24. doi:10.1088/0004-637X/779/1/24

Version: Not Applicable (or Unknown)

License: [Leiden University Non-exclusive license](#)

Downloaded from: <https://hdl.handle.net/1887/56094>

Note: To cite this publication please use the final published version (if applicable).

DISCOVERY OF THREE $z > 6.5$ QUASARS IN THE VISTA KILO-DEGREE INFRARED GALAXY (VIKING) SURVEY*

B. P. VENEMANS¹, J. R. FINDLAY², W. J. SUTHERLAND³, G. DE ROSA^{4,5}, R. G. McMAHON^{6,7},
R. SIMCOE⁸, E. A. GONZÁLEZ-SOLARES⁶, K. KUIJKEN⁹, AND J. R. LEWIS⁶

¹ Max-Planck Institute for Astronomy, Königstuhl 17, D-69117 Heidelberg, Germany; venemans@mpia.de

² Department of Physics, Durham University, South Road, Durham, DH1 3LE, UK

³ Astronomy Unit, School of Mathematical Sciences, Queen Mary, University of London, London, E1 4NS, UK

⁴ Department of Astronomy, The Ohio State University, 140 West 18th Avenue, Columbus, OH 43210, USA

⁵ Center for Cosmology & AstroParticle Physics, The Ohio State University, 191 West Woodruff Avenue, Columbus, OH 43210, USA

⁶ Institute of Astronomy, University of Cambridge, Madingley Road, Cambridge, CB3 0HA, UK

⁷ Kavli Institute for Cosmology, University of Cambridge, Madingley Road, Cambridge, CB3 0HA, UK

⁸ MIT-Kavli Center for Astrophysics and Space Research, 77 Massachusetts Avenue, Cambridge, MA 02139, USA

⁹ Leiden Observatory, Leiden University, Niels Bohrweg 2, NL-2333 CA Leiden, The Netherlands

Received 2013 July 11; accepted 2013 September 27; published 2013 November 22

ABSTRACT

Studying quasars at the highest redshifts can constrain models of galaxy and black hole formation, and it also probes the intergalactic medium in the early universe. Optical surveys have to date discovered more than 60 quasars up to $z \simeq 6.4$, a limit set by the use of the z -band and CCD detectors. Only one $z \gtrsim 6.4$ quasar has been discovered, namely the $z = 7.08$ quasar ULAS J1120+0641, using near-infrared imaging. Here we report the discovery of three new $z \gtrsim 6.4$ quasars in 332 deg² of the Visible and Infrared Survey Telescope for Astronomy Kilo-degree Infrared Galaxy (VIKING) survey, thus extending the number from 1 to 4. The newly discovered quasars have redshifts of $z = 6.60, 6.75,$ and 6.89 . The absolute magnitudes are between -26.0 and -25.5 , 0.6 – 1.1 mag fainter than ULAS J1120+0641. Near-infrared spectroscopy revealed the Mg II emission line in all three objects. The quasars are powered by black holes with masses of $\sim(1-2) \times 10^9 M_{\odot}$. In our probed redshift range of $6.44 < z < 7.44$ we can set a lower limit on the space density of supermassive black holes of $\rho(M_{\text{BH}} > 10^9 M_{\odot}) > 1.1 \times 10^{-9} \text{ Mpc}^{-3}$. The discovery of three quasars in our survey area is consistent with the $z = 6$ quasar luminosity function when extrapolated to $z \sim 7$. We do not find evidence for a steeper decline in the space density of quasars with increasing redshift from $z = 6$ to $z = 7$.

Key words: cosmology: observations – galaxies: active – quasars: general – quasars: individual (VIKING J234833.34–305410.0, J010953.13–304726.3, J030516.92–315056)

Online-only material: color figures

1. INTRODUCTION

The cosmic microwave background reveals the earliest observable structure in the universe, which dates back to the epoch of recombination at $z \sim 1100$. The next most distant observable structure represents the population of galaxies and quasars at $z \sim 7$ – 10 . The interval between $z = 1000$ and $z = 7$ contains many landmark events, such as the formation of the first stars and galaxies, the growth of the first massive black holes, and the reionization of the neutral hydrogen in the intergalactic medium (IGM). Measurements by the *Wilkinson Microwave Anisotropy Probe* give a 2σ lower bound to the epoch of reionization of $z_r = 8.2$ (Komatsu et al. 2011) but do not pin down when reionization began or ended. Another probe of the ionized state of the IGM are spectra of high redshift quasars. Already, the analysis of spectra of $z \sim 6$ quasars suggest that the epoch of reionization ended around $z \sim 6.1$ (Gnedin & Fan 2006; Becker et al. 2007).

While in recent years the evidence is pointing toward galaxies providing the required UV flux to reionize the universe (e.g., Willott et al. 2010b; Bouwens et al. 2012), the identification and study of quasars up to the highest redshifts is very important for

several reasons: (1) absorption line studies of cosmologically distributed intervening material allow the determination of the baryonic content and physical conditions (metallicity, temperature, ionization state) of the universe during the epoch of reionization (e.g., Mortlock et al. 2011; Bolton et al. 2011; Simcoe et al. 2012); (2) the number density of high redshift quasars provide constraints on the mechanisms that are required to seed and grow $>10^9 M_{\odot}$ supermassive black holes less than a Gyr after the big bang (e.g., Latif et al. 2013); and (3) high redshift quasars are generally located in luminous, massive host galaxies. By studying the host galaxies, we get insight into the formation of galaxies in the early universe (e.g., Walter et al. 2009; Wang et al. 2013).

In the last decade, more than 60 $5.7 < z \lesssim 6.4$ quasars have been discovered in various different surveys (e.g., Fan et al. 2006; Venemans et al. 2007; Jiang et al. 2008, 2009; Willott et al. 2010b; Morganson et al. 2012). The vast majority of these quasars have been discovered in optical surveys, in particular the Sloan Digital Sky Survey (SDSS; e.g., Fan et al. 2006) and the Canada–France High- z Quasar Survey (CFHQS; Willott et al. 2010b). The limitation of optical surveys that use silicon based CCD detectors is that they cannot find quasars beyond $z \sim 6.4$ as the sources become too faint in the reddest optical band of the survey (z -band) due to absorption by the intervening Ly α forest. To overcome this limit, large area surveys in near-infrared bandpasses are necessary.

* Based on observations collected at the European Southern Observatory, Chile, programs 179.A-2004, 087.A-0717, 087.A-0890 and 088.A-0897. This paper also includes data gathered with the 6.5 m Magellan Telescopes located at Las Campanas Observatory, Chile.

One of the first wide-field near-infrared surveys reaching a depth that allowed a search for the highest redshift quasars was the UK Infrared Telescope Infrared Deep Sky Survey (UKIDSS) Large Area Survey (LAS; Lawrence et al. 2007). Using the UKIDSS LAS, Mortlock et al. (2011) discovered the first quasar beyond $z > 6.5$, ULAS J1120+0641 at $z = 7.1$. This one $z \sim 7$ quasar already provides constraints on the neutral fraction of hydrogen up to $z = 7.1$ (Bolton et al. 2011; Mortlock et al. 2011), on the metallicity of the IGM (Simcoe et al. 2012) and on the formation of dust and stars in the host galaxy (Venemans et al. 2012). This shows that more quasars at $z > 6.5$ are needed.

Here we present the first $z > 6.5$ quasars discovered in the Visible and Infrared Survey Telescope for Astronomy (VISTA) Kilo-Degree Infrared Galaxy (VIKING) survey. In Section 2 we give a short description of the VIKING survey. In Section 3 we discuss the selection of high-redshift quasar candidates in the VIKING data, followed by the details of the imaging and spectroscopic observations of quasar candidates in Section 4. We continue with an overview of the results of the follow-up observations in Section 5. In Section 6 we characterize the newly discovered quasars. In Sections 7.1–7.3 we assess various sources of incompleteness and the effect on our quasar search. We discuss the implications of our results on the quasar luminosity function at $z \sim 7$ in Section 7.4. We conclude with a summary in Section 8.

All magnitudes are given in the AB system. For magnitudes obtained with VISTA, we use the Vega to AB conversions provided on the Cambridge Astronomical Survey Unit (CASU) website¹⁰: $Z_{AB} = Z_{Vega} + 0.521$, $Y_{AB} = Y_{Vega} + 0.618$, $J_{AB} = J_{Vega} + 0.937$, $H_{AB} = H_{Vega} + 1.384$, and $K_{s,AB} = K_{s,Vega} + 1.839$. An Λ -dominated cosmology with $\Omega_M = 0.28$, $\Omega_\Lambda = 0.72$, and $H_0 = 70 \text{ km s}^{-1} \text{ Mpc}^{-1}$ (Komatsu et al. 2011) is adopted.

2. SURVEY DATA

The VIKING survey is one of six public surveys (Arnaboldi et al. 2007) ongoing since late 2009 on VISTA, a 4 m wide field survey telescope located at ESO’s Cerro Paranal Observatory in Chile (Emerson et al. 2006). The telescope is equipped with the near-infrared camera VISTA InfraRed CAMera (Dalton et al. 2006), which contains 16 $2048 \times 2048 \text{ pixel}^2$ Raytheon VIRGO HgCdTe infrared detectors and has a field of view of 1.65 deg in diameter. With a pixel scale of $0\prime.34 \text{ pixel}^{-1}$, the instantaneous field of view (called a “pawprint”) is 0.6 deg^2 . Because the detectors sparsely sample the field of view, a mosaic of six “pawprints” carried out in a six-step pattern covers a continuous area of 1.5 deg^2 of the sky (a “tile”).

The VIKING survey aims to cover 1500 deg^2 spread over three extragalactic areas in five broad-band filters— Z , Y , J , H , and K_s . The details of the five broad-band filters and the limiting magnitudes of the VIKING survey are listed in Table 1. The three areas and the R.A. and decl. limits are as follows.

1. SGP: $22^{\text{h}}00^{\text{m}} < \text{R.A.} < 03^{\text{h}}30^{\text{m}}$, $-36^\circ < \text{decl.} < -26^\circ$;
2. NGP: $10^{\text{h}}30^{\text{m}} < \text{R.A.} < 15^{\text{h}}30^{\text{m}}$, $-5^\circ < \text{decl.} < +4^\circ$;
3. GAMA09: $08^{\text{h}}36^{\text{m}} < \text{R.A.} < 09^{\text{h}}24^{\text{m}}$, $-2^\circ < \text{decl.} < +3^\circ$.

The data are processed by CASU and archived at the Wide Field Astronomy Unit at the Royal Observatory in Edinburgh as part of the VISTA Data Flow System (Lewis et al. 2005, 2010). At CASU all the VISTA data are processed to science products, including astrometric and photometric calibration, for

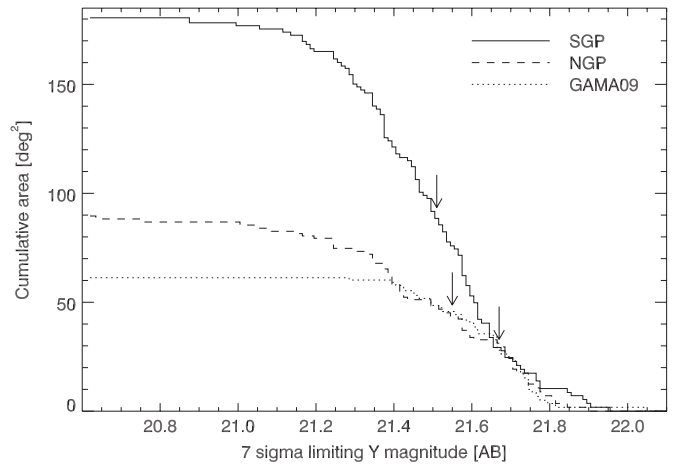


Figure 1. Cumulative area in square degrees covered by the VIKING survey in the Y-band up to 2011 March as a function of 7σ limiting magnitude. The median depth for each region is indicated by an arrow.

Table 1
Characteristics of the Filters Used in the VIKING Survey
and the Nominal 5σ Limiting Magnitudes

Filter	Central Wavelength ^a	Width ^a	Exposure Time ^b	Nominal Depth ^c
Z	0.877	0.097	480	23.1
Y	1.020	0.093	400	22.3
J	1.252	0.172	400	22.1
H	1.645	0.291	300	21.5
K_s	2.147	0.309	480	21.2

Notes.

^a Filter central wavelength and width in μm .

^b Typical exposure time per pixel in s.

^c 5σ AB magnitudes.

each night of data (Irwin et al. 2004). The stacking of pawprints into a tile is done if a suitable set of pawprints has been taken within a single Observing Block (OB). For the VIKING survey, the observations of a single tile in the five broad-band filters are spread over two OBs: in one OB, the Z -, Y - and half the J -band are taken, while the second OB consists of the H - and K_s -band images and the second half of the J -band observations. After the reduction at CASU, we thus have Z -, Y -, H -, and K_s -band images and catalogs to the full depth, while we have two separate J -band images with half the total exposure time.

The VIKING data used in this article were obtained between 2009 November and 2011 March. We downloaded the processed images and catalogs directly from CASU and band-merged the catalogs ourselves. When we had two separate J -band catalogs for the same tile, we merged the two catalogs. A search radius of $1\prime.5$ was used to merge the catalogs. The search radius is roughly three times that of the seeing measured in the VIKING data, which has a medium FWHM of $0\prime.99$. If no entry was found in a catalog, a 3σ limit was assigned to the object. The total number of tiles observed up to 2011 March for which we had at least Z -, Y -, and J -band catalogs was 44 in the GAMA09 region, 59 in the NGP, and 121 in the SGP. The total unique area covered by these tiles was 331.6 deg^2 (61.2 deg^2 in GAMA09, 89.6 deg^2 in the NGP, and 180.8 deg^2 in the SGP). The area as a function of 7σ depth in the Y-band is shown in Figure 1. The median 7σ Y-band depths are 21.67, 21.55, and 21.51 for the GAMA09, NGP, and SGP regions, respectively.

¹⁰ <http://casu.ast.cam.ac.uk/>

3. CANDIDATE SELECTION

We selected candidate high redshift ($z \gtrsim 6.5$) quasars from the band-merged catalogs¹¹ by applying the following steps.

1. Objects should be detected in the Y -band with a signal-to-noise ratio (S/N) of at least $(S/N)_Y > 7$. We also required that the object is detected in at least one other band. For all bands we use aperture-corrected magnitudes measured in an aperture with a radius of $1''.0$ (labeled aperMag3 in the catalogs).
2. We only consider point sources that we define as objects having a probability of being a galaxy (p_{Galaxy}) of $p_{\text{Galaxy}} < 0.95$ (see Irwin et al. 2004; González-Solares et al. 2008 for details on the morphological parameters). This selection makes sure that most real point sources are selected with a manageable fraction of galaxies (see also Section 7.2 and Findlay et al. 2012).
3. The aperture-corrected magnitudes in the Y band had to be independent of the size of aperture used to within 0.2 mag. This was forced by applying $\text{aperMag1} - \text{aperMag3} < 0.2$ and $\text{aperMag3} - \text{aperMag4} < 0.2$. Removing this criterion did not increase the number of candidate quasars, but did add more artifacts to our candidate lists.
4. Because $z > 6.5$ quasars occupy a unique region in color space, we can isolate potential quasars in the catalogs by introducing color criteria. We applied two sets of color criteria to select $z > 6.5$ quasar candidates, a conservative color selection, and an extended color selection. The conservative color selection minimizes the number of foreground objects wrongly selected as candidate quasars and is based on the work of Findlay et al. (2012). The extended color criteria maximize the completeness of the high redshift quasar selection, without purposely selecting foreground objects. The conservative color criteria are as follows.

$Z - Y \geq 1.25$ AND $-0.5 < Y - J \leq 0.5$ AND $(Z > Z_{\text{lim},3\sigma}$ OR $Z - Y > 0.75 \times (Y - J) + 1.45$) AND $-0.5 < Y - K < 1.3$ AND undetected in u, g, r and i (when optical imaging is available).

The extended color criteria are as follows.

$Z - Y \geq 1.1$ AND $-0.5 < Y - J \leq 0.5$ AND $(Z > Z_{\text{lim},3\sigma}$ OR $Z - Y > Y - J + 0.7)$ AND $-0.5 < Y - K < 1.0$ AND $J - K < 0.8$ AND undetected in u, g, r, i (when optical imaging is available).

Our color criteria are illustrated in Figure 2.

5. Detector 16 has a time-varying quantum efficiency. As a result, the flat fielding is not accurate and the detector produces a large number spurious detections. We therefore ignore objects that originated from detector 16 in one pawprint and were not independently confirmed in another pawprint.
6. To check the magnitudes listed in the catalogs and especially nondetections in the Z -band, we performed aperture photometry in each of the VIKING images at the location of the candidate. If the colors measured did not fulfill the color criteria listed above, the object was removed from our candidate list.
7. The final step was visually inspecting all candidates in order to remove any remaining spurious objects. Most of the eliminated objects were near the edge or just outside

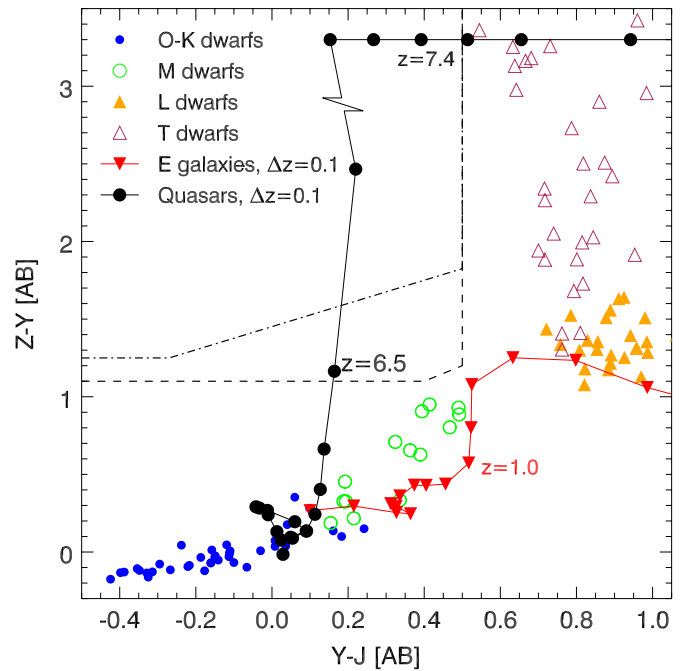


Figure 2. $Z - Y$ vs. $Y - J$ diagram illustrating our color selection criteria. The dashed line shows our extended criteria, while the dash-dotted line illustrates our conservative color criteria. Also plotted are simulated colors of main sequence stars (small, blue dots), M dwarfs (green, open circles), L dwarfs (yellow, solid triangles), T dwarfs (open, maroon triangles), elliptical galaxies (red, upside-down triangles), and quasars (black, solid points) from Hewett et al. (2006). Quasars above $z \gtrsim 6.4$ – 6.5 occupy a region in the color-color diagram that is well separated from foreground objects. Quasars above $z > 6.6$ become quickly very faint in the Z -band and have $Z - Y \gg 3$. We truncated the quasar track between $z = 6.6$ and $z = 7.2$ to show the evolution of the $Y - J$ color at the highest redshifts. At redshifts $z \gtrsim 7.4$ – 7.5 quasars become too red in $Y - J$ color to separate them from brown dwarfs in color space.

(A color version of this figure is available in the online journal.)

the Z -band image, or on diffraction spikes. This step approximately halved the number of candidates on our lists.

With the conservative color criteria we selected 43 objects in the three different regions observed by VIKING: 7 objects in GAMA09, 18 in the NGP, and 18 in the SGP. We applied our extended color selection to the NGP region and further selected another 42 objects. We loosely ranked the objects according to their $Z - Y$ color, i.e., objects with a higher $Z - Y$ had a higher priority for follow-up observations.

4. FOLLOW-UP OBSERVATIONS

4.1. ESO NTT/EFOSC2 Imaging

On 2011 June 26–29 we observed quasar candidates from VIKING with the European Southern Observatory’s Faint Object Spectrograph and Camera 2 (EFOSC2; Buzzoni et al. 1984) on the 3.58 m ESO New Technology Telescope (NTT). We observed in filters Gunn i (filter #705, hereafter I_N) and Gunn z (filter #623, hereafter Z_N).

Images taken with the Z_N filter were calibrated using stars within the EFOSC2 field of view. Using the filter transmission curves, the CCD efficiency and stellar spectra from the BPGS spectroscopic atlas¹² (Gunn & Stryker 1983), we established a relation between the Z_N and the VIKING Z and Y magnitudes of $Z_N = Z - 0.135 \times (Z - Y) + 0.01$. In fields with SDSS

¹¹ For a detailed description of all the parameters in the catalogs that are generated at CASU, see <http://casu.ast.cam.ac.uk/surveys-projects/vista/technical/catalogue-generation>

¹² <http://www.stsci.edu/hst/observatory/cdbs/bpgs.html>

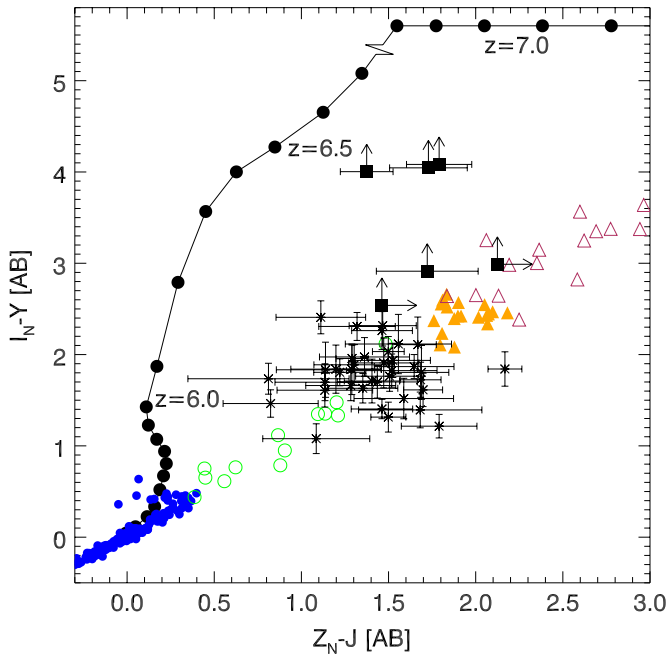


Figure 3. $I_N - Y$ vs. $Z_N - J$ diagram showing the results of the follow-up observations with the NTT. Similar to Figure 2, colors of simulated stars, galaxies, and quasars are also shown (see the caption of Figure 2 for an explanation of the symbols). The value of the $I_N - Y$ color of quasars above $z > 6.7$ have been reduced to $I_N - Y = 5.6$ in order to display the change in $Z_N - J$ color of quasars with redshift more clearly. The small stars with error bars represent candidates detected in the I_N images and were identified as foreground stars. The six filled squares are candidates that were not detected in the I_N images and therefore remained good high-redshift quasar candidates. These objects were our prime targets for follow-up spectroscopy. (A color version of this figure is available in the online journal.)

coverage (the NGP and GAMA09 regions), the I_N images were calibrated using the relation (derived from synthesized colors of the BPGS stars) $I_N = i_{SDSS} - 0.4 \times (i_{SDSS} - z_{SDSS})$. Observations in the I_N filter of candidates in the SGP, for which no optical photometry of nearby stars was available, were calibrated using the spectrophotometric standard stars LTT1020, LTT6248, and LTT9239 (Hamuy et al. 1992, 1994) that were observed in the evening and morning twilight.

During the NTT run we observed 18 quasar candidates that were selected with the conservative color criteria and 20 sources that fulfilled the extended color criteria. To fill gaps in the nights, we also targeted seven objects that fell just outside the color selection and/or had a Y -band detection just below the $(S/N)_Y = 7$ limit.

Individual images had an exposure time of either 600 s or 900 s, and the total exposure time per source varied from 600 s to 8100 s. We observed 45 objects in the I_N filter, and 8 of those were also observed in the Z_N filter. Generally, if an object showed a clear detection in the initial I_N images, we stopped observing it. Objects not detected in I_N were prioritized for deeper I_N and Z_N imaging. The results of the EFOC2 photometry are listed in Table 2 and are shown in Figure 3.

Of the 45 objects we observed, 6 remained undetected in the I_N -band (see Section 5). These sources were targets for our follow-up spectroscopy.

4.2. VLT/FORS2 Spectroscopy

Between 2011 July 22 and 2011 August 20 we obtained spectra for four of the six that remained undetected in I_N images.

Table 2
Photometry Obtained with EFOC2 on the NTT

Name	R.A. (J2000)	Decl. (J2000)	$I_{N,AB}$	$Z_{N,AB}$
J0109–3047	01 ^h 09 ^m 53 ^s .13	–30°47′26″.3	>25.27	22.93 ± 0.16
J0125–3016	01 ^h 25 ^m 34 ^s .44	–30°16′27″.4	22.82 ± 0.11	...
J0221–3139	02 ^h 21 ^m 46 ^s .08	–31°39′49″.4	22.35 ± 0.08	...
J0223–3208	02 ^h 23 ^m 31 ^s .00	–32°08′37″.7	22.73 ± 0.10	...
J0223–3144	02 ^h 23 ^m 53 ^s .26	–31°44′26″.6	23.37 ± 0.26	...
J0259–3100	02 ^h 59 ^m 42 ^s .43	–31°00′54″.4	22.57 ± 0.12	...
J0305–3150	03 ^h 05 ^m 16 ^s .92	–31°50′56″.0	>24.97	22.12 ± 0.07
J0305–3400	03 ^h 05 ^m 58 ^s .11	–34°00′01″.9	22.56 ± 0.10	...
J0322–3350	03 ^h 22 ^m 13 ^s .93	–33°50′25″.2	23.26 ± 0.24	...
J0914+0155	09 ^h 14 ^m 19 ^s .52	+01°55′52″.0	23.70 ± 0.29	...
J1146+0145	11 ^h 46 ^m 26 ^s .56	+01°45′48″.8	22.73 ± 0.10	...
J1147+0126	11 ^h 47 ^m 24 ^s .90	+01°26′34″.6	22.94 ± 0.12	...
J1149–0046	11 ^h 49 ^m 35 ^s .20	–00°46′00″.8	22.87 ± 0.12	...
J1151+0118	11 ^h 51 ^m 31 ^s .68	+01°18′05″.3	23.67 ± 0.22	...
J1154+0141	11 ^h 54 ^m 39 ^s .84	+01°41′53″.3	>24.18	>22.81
J1156–0007	11 ^h 56 ^m 42 ^s .26	–00°07′58″.1	>24.49	>23.22
J1211+0007	12 ^h 11 ^m 43 ^s .09	+00°07′31″.2	22.95 ± 0.14	...
J1213+0159	12 ^h 13 ^m 21 ^s .91	+01°59′45″.7	23.34 ± 0.16	...
J1213+0200	12 ^h 13 ^m 34 ^s .80	+02°00′32″.7	23.47 ± 0.19	...
J1218+0051	12 ^h 18 ^m 24 ^s .54	+00°51′12″.9	22.96 ± 0.15	...
J1218+0106	12 ^h 18 ^m 46 ^s .88	+01°06′24″.2	22.65 ± 0.12	...
J1219+0003	12 ^h 19 ^m 12 ^s .11	+00°03′26″.4	22.46 ± 0.07	...
J1412+0128	14 ^h 12 ^m 33 ^s .63	+01°28′10″.0	23.10 ± 0.09	...
J1413+0139	14 ^h 13 ^m 41 ^s .55	+01°39′55″.5	23.41 ± 0.26	...
J1414+0126	14 ^h 14 ^m 42 ^s .14	+01°26′19″.7	23.15 ± 0.11	...
J1418–0018	14 ^h 18 ^m 11 ^s .45	–00°18′53″.1	23.07 ± 0.15	...
J1418+0109	14 ^h 18 ^m 31 ^s .42	+01°09′33″.9	23.34 ± 0.13	...
J1419–0100	14 ^h 19 ^m 56 ^s .00	–01°00′15″.3	23.38 ± 0.14	...
J1425–0054	14 ^h 25 ^m 36 ^s .77	–00°54′29″.5	22.39 ± 0.06	...
J1429+0142	14 ^h 29 ^m 27 ^s .27	+01°42′56″.9	22.94 ± 0.08	...
J1431+0029	14 ^h 31 ^m 33 ^s .72	+00°29′00″.0	23.83 ± 0.15	22.58 ± 0.14
J1434–0003	14 ^h 34 ^m 09 ^s .86	–00°03′45″.4	23.00 ± 0.09	...
J1447+0113	14 ^h 47 ^m 05 ^s .74	+01°13′46″.4	23.15 ± 0.10	...
J1450–0023	14 ^h 50 ^m 12 ^s .55	–00°23′45″.7	23.24 ± 0.10	...
J1450+0100	14 ^h 50 ^m 20 ^s .11	+01°00′22″.1	22.37 ± 0.05	...
J1451+0021	14 ^h 51 ^m 37 ^s .09	+00°21′33″.4	23.23 ± 0.09	...
J2214–3134	22 ^h 14 ^m 59 ^s .28	–31°34′39″.0	23.77 ± 0.13	...
J2215–3145	22 ^h 15 ^m 36 ^s .00	–31°45′44″.6	20.97 ± 0.03	...
J2218–3154	22 ^h 18 ^m 57 ^s .36	–31°54′30″.0	>24.77	...
J2222–3129	22 ^h 22 ^m 12 ^s .24	–31°29′42″.4	23.52 ± 0.19	...
J2223–3158	22 ^h 23 ^m 28 ^s .02	–31°58′35″.6	23.29 ± 0.11	22.48 ± 0.14
J2226–3124	22 ^h 26 ^m 58 ^s .29	–31°24′45″.3	23.59 ± 0.10	...
J2229–3057	22 ^h 29 ^m 16 ^s .29	–30°57′22″.8	23.64 ± 0.16	23.07 ± 0.30
J2348–3054	23 ^h 48 ^m 33 ^s .34	–30°54′10″.0	>25.13	22.97 ± 0.13
J2358–3355	23 ^h 58 ^m 23 ^s .36	–33°55′21″.1	23.03 ± 0.14	...

Note. Objects that were not detected in the images have the 3σ limiting magnitude.

We used the FOCAL Reducer/low dispersion Spectrograph 2 (FORS2; Appenzeller et al. 1998) on the 8.2 m Very Large Telescope (VLT) Antu. The candidates were observed through the 600z holographic grism with a 1/3 wide longslit. The pixels were 2×2 binned to decrease the readout time and noise, giving a spatial scale $0''.25 \text{ pixel}^{-1}$ and a dispersion of $1.62 \text{ \AA pixel}^{-1}$. Between exposures the pointing of the telescope was shifted by $\sim 10''$ along the slit for more accurate sky subtraction. The position angle of the slit was set to include a nearby star that could provide the trace of the spectrum.

On 2011 July 22, 23, and 29 candidate VIKING J234833.34–305410.0 (hereafter J2348–3054) was observed for a total of 6750 s under varying conditions. On July 22 and 23 the seeing varied between $1''.5$ and $2''.5$ with clear sky.

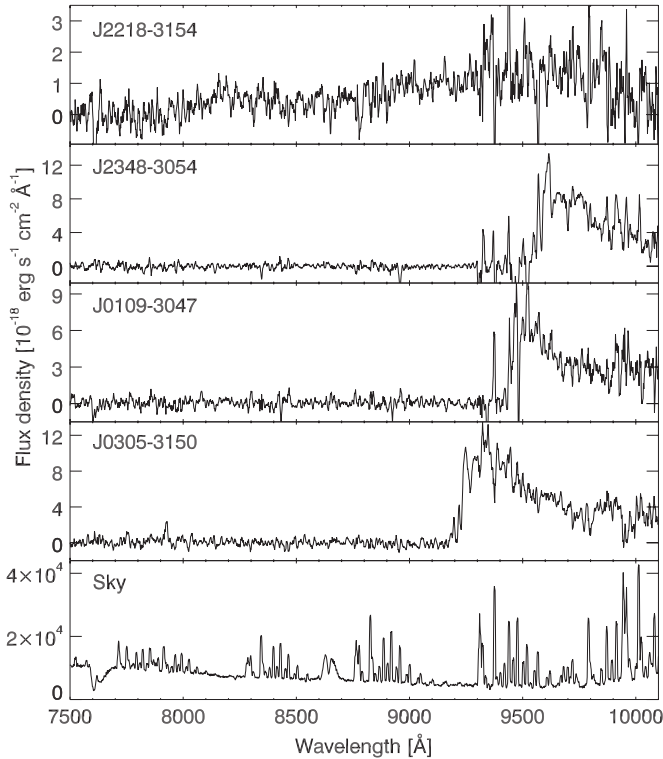


Figure 4. VLT/FORS2 spectra of four-high redshift quasar candidates that remained undetected in the I_N images. Below the four objects a sky spectrum is plotted. The spectra are boxcar averaged over five pixels. The spectra were not corrected for slit losses. Three of the targets (J2348–3054, J0109–3047, and J0305–3150) show a continuum decrement above ~ 9200 Å, which is characteristic for quasars at $z \gtrsim 6.5$. The fourth target (J2218–3154) does not show a break in the continuum and is probably an L dwarf. Identifying the peak of the quasar spectra as Ly α (1216 Å), the estimated redshifts for the quasars are $z \sim 6.9$ (J2348–3054), $z \sim 6.8$ (J0109–3047), and $z \sim 6.6$ (J0305–3150).

On July 29 the seeing was $1''.1$ – $1''.3$ while there were some thin clouds. Candidate VIKING J010953.13–304726.3 (hereafter J0109–3040) was observed for 2280 s on 2011 July 22. Conditions were clear with a seeing around $1''.2$. Six exposures totaling 4500 s were taken of candidate VIKING J030516.92–315056.0 (hereafter J0305–3150) on 2011 August 13 and 20. The seeing was around $0''.7$, and there were some thin clouds. Finally, candidate VIKING J221857.36–315430.0 (hereafter J2218–3153) was observed on 2011 August 20 for 1350 s through thin clouds and with a seeing of $0''.6$.

The data reduction, which included bias subtraction, flat fielding using lamp flats, and sky subtraction, was done using custom written routines in IDL. For the wavelength calibration, exposures of He, HgCd, and Ne arc lamps were obtained. The wavelength calibration was checked using sky emission lines. The typical rms of the wavelength calibration was better than 0.6 Å. The spectra cover roughly the wavelength range 7100 Å– 10300 Å. Observations with a $5''$ slit of the spectrophotometric standard star LTT1020 (Hamuy et al. 1992, 1994) were used for the flux calibration. The flux calibration was found to be highly uncertain above 10100 Å due to a lack of flux density values for LTT1020 in the literature above this value. We therefore ignore the spectra above this wavelength. The FORS2 spectra are shown in Figure 4.

4.3. VLT/X-Shooter Observations

To increase the wavelength coverage of our spectroscopy to the near-infrared, we observed two of our spectroscopic targets,

Table 3
Photometric Properties and Derived Parameters of the Three $z > 6.5$ Quasars

	J2348–3054	J0109–3047	J0305–3150
R.A. (J2000)	23 ^h 48 ^m 33 ^s .34	01 ^h 09 ^m 53 ^s .13	03 ^h 05 ^m 16 ^s .92
Decl. (J2000)	−30°54′10″.0	−30°47′26″.3	−31°50′56″.0
$Z_{N,AB}$	22.97 ± 0.13	22.93 ± 0.16	22.12 ± 0.07
Z_{AB}	>23.42	>22.98	23.10 ± 0.35
Y_{AB}	21.11 ± 0.08	21.22 ± 0.14	20.89 ± 0.07
J_{AB}	21.14 ± 0.08	21.27 ± 0.16	20.68 ± 0.07
H_{AB}	20.80 ± 0.13	21.03 ± 0.17	20.72 ± 0.11
$K_{s,AB}$	20.51 ± 0.10	...	20.27 ± 0.09
z_{MgII}	$6.886^{+0.009}_{-0.008}$	$6.745^{+0.010}_{-0.009}$	6.604 ± 0.008
M_{1450}	-25.72 ± 0.14	-25.52 ± 0.15	-25.96 ± 0.06
$M_{BH} (M_{\odot})$	$(2.1 \pm 0.5) \times 10^9$	$(1.5 \pm 0.4) \times 10^9$	$(1.0 \pm 0.1) \times 10^9$

Note. Magnitude limits are 3σ .

J2348–3054 and J0109–3040, with the medium resolution spectrograph X-Shooter (Vernet et al. 2011) on the Cassegrain focus of the 8.2 m VLT Kueyen (UT2) on 2011 August 19–21 and on 2011 November 24. X-Shooter consists of three spectrographs, each covering a different wavelength region. The three arms and wavelength coverage of the instrument are as follows: UVB (3000 Å–5595 Å), VIS (5595 Å–10240 Å), and NIR (10240 Å–24800 Å). Given the extreme red colors of our targets, we ignored the UVB arm. The slit length in the VIS and NIR arm was $11''$, and the pixel scales are $0''.16$ pixel $^{-1}$ and $0''.21$ pixel $^{-1}$, respectively. The slit width used for the observations ranged between $0''.9$ – $1''.5$ in the VIS arm and between $0''.9$ – $1''.2$, with the width adjusted to counter periods of bad seeing. The resulting resolution varied between $R = 5400$ – 8800 in the VIS arm and between $R = 4000$ – 5000 partly in the NIR arm. Observing conditions on 2011 August 19 were variable with the seeing in the optical ranging from $0''.9$ to $\sim 1''.3$ and some thin clouds. For flux calibration, observations of the spectrophotometric standard stars LTT7987 and Feige110 were obtained (Hamuy et al. 1994; Vernet et al. 2010).

We observed J0109–3040 for 14,400 s in August and for 7200 s in November. J2348–3054 was observed in August only for 8783 s. We made use of the X-Shooter pipeline version 1.3.7 (Modigliani et al. 2010) to reduce the data to two-dimensional rectified wavelength-calibrated spectra. The extraction of the spectra and the flux calibration were performed with custom-made programs in IDL. We scaled the one-dimensional spectra to match the observed infrared colors from VIKING (listed in Table 3). We do note that the $Y - J$ color of the quasars derived from the X-Shooter spectra is 0.2 mag redder as compared to the catalog colors (Table 3). A possible reason is that the light that the Y band is measuring ends up partly in the VIS arm and in the NIR arm. This causes additional uncertainties in the flux calibration around $1 \mu\text{m}$. In the top two panels of Figure 5 we show the reduced X-Shooter spectra.

4.4. Magellan/FIRE Observations

We observed J0305–3150 using the Folded-Port Infrared Echellette (FIRE; Simcoe et al. 2008, 2010) on the Magellan Baade telescope on four separate observing runs between 2011 November and 2012 January. FIRE produces spectra with $R = 6000$ ($\Delta v = 50 \text{ km s}^{-1}$) over the full 0.82 – $2.51 \mu\text{m}$ wavelength range. The data were taken in generally clear conditions with a seeing of $0''.8$ FWHM or better, with a total integration time of 26,400 s.

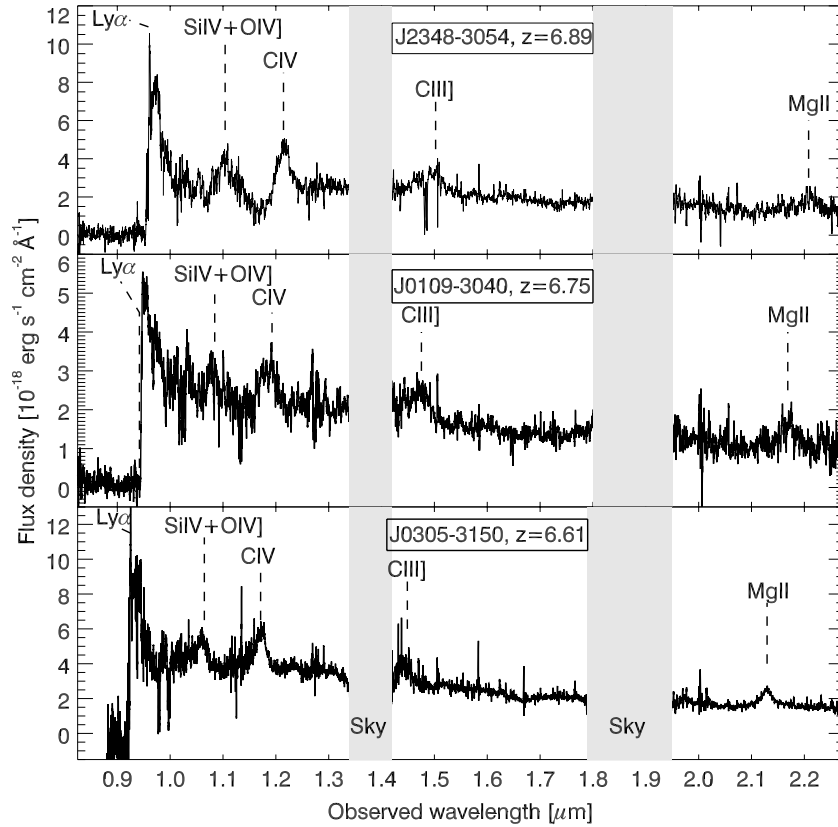


Figure 5. X-Shooter (top two panels) and FIRE (bottom panel) medium resolution, infrared spectra of the three new $z > 6.5$ quasars. The spectra are smoothed over 11 pixels to better show the broad emission lines. Various strong emission lines in the spectra are marked.

We reduced each echelle frame using a customized IDL suite (FIREHOSE) designed for FIRE data. The pipeline produces an order-by-order two-dimensional spectral model of the sky using the principles outlined in Kelson (2003) and subtracts this from the flattened data frames. Wavelength solutions are obtained using tabulated values of the OH sky emission lines imprinted on the same frames. We interspersed observations of A0V stars for telluric correction, which was performed using the algorithms of Vacca et al. (2003) as implemented in the Spextool software package (Cushing et al. 2004). Finally, the corrected and flux calibrated orders for all exposures were combined into a single one-dimensional spectrum, with each individual sampling weighted by its squared S/N for an optimum S/N composite (Figure 5).

5. RESULTS

We obtained I_N imaging of 45 high redshift quasar candidates with the NTT and Z_N imaging for more promising candidates. Based on the colors (Figure 3), 39 objects could be rejected as quasar candidates after the NTT imaging as they are likely to be late M or early L dwarfs. This is much as expected, since these objects are numerous and a small fraction of them are expected to scatter into our selection region due to random photometric errors. Only six quasar candidates were undetected in the I_N images (Figure 3 and Table 2) and could not immediately be identified as a foreground object. Five of these satisfied the conservative color criteria, while the sixth source, J2218–3153, was a filler object with a $(S/N)_Y < 7$. Four candidates, including J2218–3153, were spectroscopically observed with FORS2 (Figure 4).

The spectrum of J2218–3153 shows a smoothly rising spectrum, and the source is most likely an early L dwarf. The FORS2 spectra of the three other objects, J2348–3054, J0109–3047, and J0305–3150, show a strong continuum decrement between 9200 Å and 9600 Å and were identified as quasars at $z = 6.6$ –6.9. For these three sources, we obtained near-infrared spectroscopy (Figure 5) to more accurately determine the redshift and estimate the properties of the quasars. In Section 5.1 we describe how we derive the various quasar properties. These results are discussed in Section 6 and summarized in Table 3.

Based on the available photometry, the two remaining candidates, J115439.84+014153.3 and J115642.26–000758.1, could either be high redshift quasars or late-type stars (M, L, or T dwarfs). Spectroscopic observations of these sources are needed to determine their nature.

5.1. M_{1450} , Redshift, and Black Hole Mass Estimates

M_{1450} . The absolute magnitude of the quasars at a rest-frame wavelength of 1450 Å (M_{1450}) can be derived by measuring the flux density in the near-infrared spectra at the redshifted wavelength $1450 \times (1+z)$ Å. The redshifts of the quasars of $z = 6.6$ –6.9 shift the rest-frame wavelength of 1450 Å to an observed wavelength of 1.10–1.15 μm, which is roughly between the Y- and J-band. Because the Y – J colors measured from the X-Shooter spectra do not agree with the quasar colors from the catalogs (see Sections 4.3), we scale the spectra of J2348–3054 and J0109–3040 to either the catalog Y or J magnitude and compute M_{1450} twice from the flux density that we measure in the spectra at the appropriate wavelength. The absolute magnitudes of these two quasars listed in Table 3 are the

average of the two values, and the uncertainties are the standard deviation of the mean. This way the uncertainty in the absolute magnitude includes the issues with the flux calibration. For J0305–3150 the $Y - J$ color measured from the FIRE spectrum was consistent with the one from the catalog, and we could measure the flux density at 1450 Å in the rest-frame directly in the spectrum.

Black Hole Mass. In De Rosa et al. (2013) the infrared spectra of the quasars were fitted to estimate the black hole mass and the redshift of the Mg II $\lambda 2799$ line. For the details of the fitting, we refer to De Rosa et al. (2013). Here we will give a short summary of the fitting procedures. De Rosa et al. (2013) modeled the quasar continuum as the sum of the power-law emission from the active galactic nucleus, the Balmer continuum emission (Grandi 1982), and the Fe II and Fe III emission line forest (Vestergaard & Wilkes 2001). The probability of the continuum model parameters was estimated using a grid-based approach. To fit the Mg II line, De Rosa et al. (2013) sampled the obtained continuum probability distribution N times by using a Monte Carlo rejection method. For each sample, the corresponding continuum was subtracted from the observed spectrum and the emission line was fitted, assuming a Gaussian profile, using a χ^2 minimization routine.

The resulting distribution of black hole masses was estimated by combining the N continuum luminosities at $\lambda_{\text{rest}} = 3000$ Å with the FWHM measured for the Mg II line: $M_{\text{BH}} = 10^{6.86} (\text{FWHM}(\text{Mg II})/1000)^2 (\lambda L_{3000\text{Å}}/10^{44})^{0.5}$ (Vestergaard & Osmer 2009), where $\text{FWHM}(\text{Mg II})$ is the FWHM of the Mg II line in km s^{-1} and $\lambda L_{3000\text{Å}}$ is the nuclear continuum luminosity at $\lambda_{\text{rest}} = 3000$ Å in $\text{erg s}^{-1} \text{Å}^{-1}$.

The uncertainties concerning the black hole mass estimates listed in Section 6 only include the uncertainties from the continuum modeling and from the line fitting. Systematic uncertainties, such as the scatter in the scaling relation of 0.55 dex, are not taken into account.

Redshift. We use the peak of the Mg II emission line as measured by De Rosa et al. (2013) to obtain the redshift of the quasars. The redshifts derived this way have been corrected for the velocity shift of $-97 \pm 269 \text{ km s}^{-1}$ as found between Mg II and the systemic redshift of lower redshift quasars as traced by the [O III] $\lambda 5008$ emission line (Richards et al. 2002b). The uncertainty in this shift is added in quadrature to the statistical redshift uncertainty of the Gaussian fit of the emission line.

6. PROPERTIES OF INDIVIDUAL QUASARS

6.1. J2348–3054

This source was selected with $Y - J = -0.03 \pm 0.11$ and $Z - Y > 2.31$ (see Table 3). With the NTT we observed the source for 5400 s in I_N and for 3600 s in Z_N . The source was not detected in the I_N image, implying $I_N > 25.13$ and $I_N - Y > 4.02$. Combined with a detection in the Z_N image of $Z_N = 22.97 \pm 0.13$, we could identify this object as a probable high redshift quasar with $6.5 < z \lesssim 7$ and rule out a foreground identification of the source (Figure 3).

The discovery spectrum taken with VLT/FORS2 (Figure 4) shows a source with continuum detected in the red part and a sharp break between 9500 Å and 9600 Å. We interpreted this feature as the onset of absorption in the IGM shortward of the Ly α line in the quasar and estimated a redshift of $z \sim 6.9$. The VLT/X-Shooter spectrum (Figure 5) shows several strong emission lines, such as Si IV $\lambda 1397 + \text{O IV} \lambda 1402$, C IV $\lambda 1549$, C III] $\lambda 1909$, and Mg II $\lambda 2799$. A fit of the Mg II line produced

a more accurate redshift of $z = 6.886^{+0.009}_{-0.008}$. The continuum blueward of the C IV emission line is partly absorbed, suggesting that this quasar is a broad absorption line (BAL) quasar.

Extrapolating the continuum above the C IV absorption, we measure an absolute magnitude at 1450 Å in the rest-frame of $M_{1450} = -25.72 \pm 0.14$, which is approximately 1 mag fainter than ULAS J1120+0641 at $z = 7.1$ (Mortlock et al. 2011).

The black hole mass that De Rosa et al. (2013) derive from the width of the Mg II emission line and the strength of the continuum is $M_{\text{BH}} = (2.1 \pm 0.5) \times 10^9 M_{\odot}$.

6.2. J0109–3040

In our catalogs, this source was selected with colors $Y - J = -0.05 \pm 0.21$ and $Z - Y > 1.76$ (Table 3). We observed the source for 8100 s in I_N and 3600 s in Z_N with the NTT. Similar to J2348–3054, J0109–3040 remained undetected in the deep I_N image, suggesting a very red $I_N - Y > 4.05$. The $Z_N - J$ was slightly (~ 0.2 mag) bluer than that of J2348–3054, again ruling out a foreground interpretation of the optical–infrared colors. The FORS2 spectrum revealed an object with a strong continuum break around 9400 Å–9500 Å (Figure 4), and we identified the source as a quasar at $z \sim 6.8$.

The X-Shooter spectrum (Figure 5) shows several strong emission lines, including Si IV + O IV, C III], and Mg II, from which we derive a redshift of $z_{\text{Mg II}} = 6.745^{+0.010}_{-0.009}$. The Ly α emission line is completely absorbed. Despite the lack of Ly α emission, the continuum at wavelengths shortward of C IV is not absorbed and, unlike J2348–3054, J0109–3040 is not a BAL.

From the X-Shooter spectrum we can directly measure the flux density at 1450 Å in the rest frame. We find that the quasar has $M_{1450} = -25.52 \pm 0.15$. The uncertainty in the absolute magnitude includes the moderate S/N of the Y and J VIKING magnitudes that were used to derive the absolute flux calibration of the spectrum. The absolute magnitude of $M_{1450} = -25.52$ makes it the faintest quasar in our sample and 1.5–2.5 mag fainter than the $z \sim 6$ quasars found in the main SDSS survey (Fan et al. 2006). Although the quasar is fainter in the continuum, the black hole mass of $M_{\text{BH}} = (1.5 \pm 0.4) \times 10^9 M_{\odot}$ is similar to that of J2348–3054 (De Rosa et al. 2013).

6.3. J0305–3150

J0305–3150 was the only quasar in our sample that was detected in the VIKING Z image. The $Z - Y$ color of $Z - Y = 2.21 \pm 0.36$ was red enough to fulfill the conservative color selection. Over the three observing nights with the NTT we exposed the source for a total of 3600 s through the I_N filter and for 2700 s through Z_N . While the $I_N - Y$ color we measured was similar to that of the other two quasars ($I_N - Y > 4.08$; Table 3), the $Z_N - J$ was 0.2–0.4 mag bluer. This was an indication that the redshift is lower than that of the other quasars. Of the three new quasars, this object had the brightest (observed) magnitudes, being around 0.5 mag brighter in J than the other two quasars.

The FORS2 observations showed a quasar spectrum with a break around ~ 9200 Å, corresponding to a Ly α redshift of $z \sim 6.6$. The redshift was more accurately determined using the FIRE spectrum of the quasar. The infrared spectrum showed the same emission lines as in the other two VIKING quasars. A fit to the Mg II emission line gives a redshift of $z = 6.604 \pm 0.008$. The absolute magnitude of this quasar is $M_{1450} = -25.96 \pm 0.06$, making it the brightest of the new quasars, but still ~ 0.6 mag fainter than ULAS J1120+0641.

The wavelength coverage of the FIRE spectrum allowed De Rosa et al. (2013) to estimate the mass of the black hole.

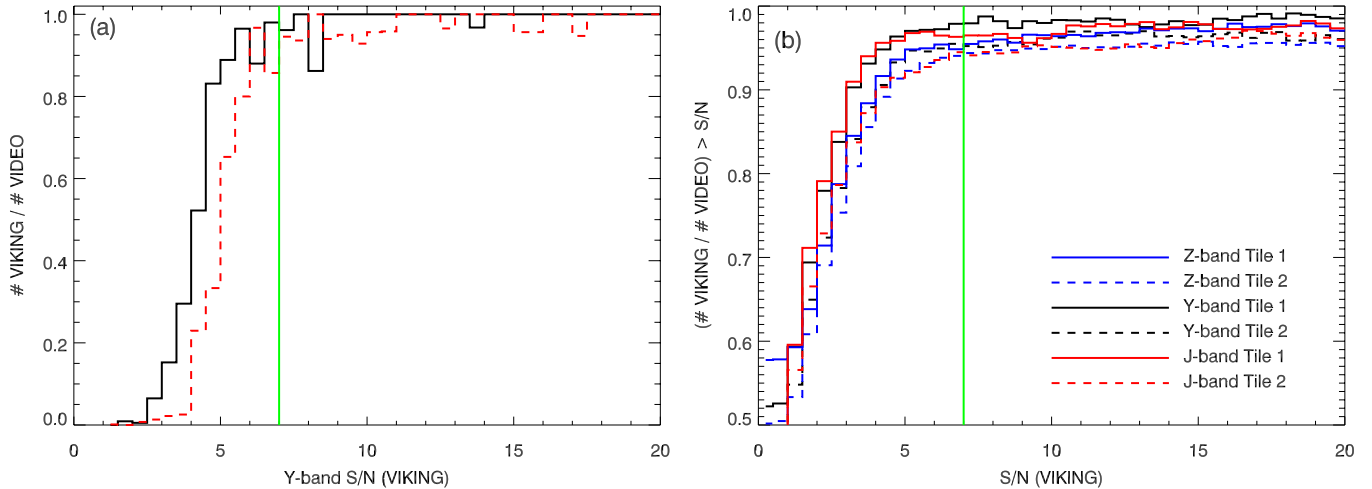


Figure 6. (a) Completeness of the Y-band counts as a function of Y-band S/N. The fractions are derived by comparing the counts in the VIKING catalogs with the counts in the VIDEO catalog in similar magnitude ranges. The solid and dashed histograms represent two different VIKING tiles that (partly) overlap with the VIDEO data. The vertical solid line indicates the 7σ limit we applied to the VIKING catalogs. (b) VIKING Z-, Y-, and J-band catalog completeness as a function of limiting S/N for the two tiles overlapping with the VIDEO survey. Down to 7σ the VIKING catalogs are 94%–98% complete.

(A color version of this figure is available in the online journal.)

Based on the fit to the continuum and on the Gaussian modeling of the Mg II emission line, they derive a $M_{\text{BH}} = (1.0 \pm 0.1) \times 10^9 M_{\odot}$.

7. THE QUASAR LUMINOSITY FUNCTION AT $z \sim 7$

In this section we will compare our discovery of three quasars at $z > 6.5$ in 331.6 deg^2 that was covered by VIKING with the expected number of quasars based on the quasar luminosity function at $z \sim 6$. We first estimate the completeness of the catalogs and the efficiency of the point source selection (Sections 7.1 and 7.2). We then test the efficiency and completeness of our conservative and extended color selections (Section 7.3). In Section 7.4 we apply the completeness calculations to the number density of VIKING quasars and compare those with the predictions based on the $z = 6$ quasar luminosity function extrapolated to $z > 6.5$.

7.1. Catalog Completeness

To assess how complete the VIKING catalogs are as a function of limiting S/N, we need to compare the detected number of sources in the VIKING catalogs with the expected number of sources. To determine the number of objects that are expected in the VIKING images, we make use of the first data release of the VISTA Deep Extragalactic Observations (VIDEO) survey (Jarvis et al. 2013). The VIDEO data overlap with test data from the VIKING survey in the Canada–France–Hawaii–Telescope–Legacy Survey Deep-1 field. Since the VIDEO survey is 2.2–2.6 mag deeper than VIKING in all five VISTA bands and highly complete down to the limits of the VIKING survey (see Table 3 in Jarvis et al. 2013), we can take the VIDEO catalogs to determine which fraction of the sources is recovered in the VIKING catalogs. The VIDEO area is partly covered by two different VIKING pointings, with the total overlap roughly 1 deg^2 . The two VIKING tiles that overlap the VIDEO region have similar characteristics (average limiting magnitudes, seeing, etc.) as those of a typical VIKING tile.

Our calculation of the completeness of the VIKING catalogs as a function of S/N was done in the following way. First, we computed for a given S/N what the corresponding magnitude range was. We then counted the number of objects within that

magnitude range in the VIDEO catalogs and compared that to the number of sources with a match in the VIKING catalogs. In Figure 6(a) we show the fraction of objects in the VIDEO Y-band catalog that are recovered in the VIKING catalog. The VIKING catalogs are over 95% complete down to a S/N ~ 5 . The completeness as function of limiting S/N is plotted in Figure 6(b). We computed the number of VIDEO sources above the magnitude corresponding to the VIKING S/N limit and counted the fraction of sources that had a match above the S/N limit in the VIKING catalog. We have six independent measurements of the completeness (two VIKING pointings with three filters each), and the completeness above a S/N > 7 was in the range 94.4%–97.9% with an average of 95.7%.

Based on the counts in the deeper VIDEO catalogs, we recover around 96% of the objects in the VIKING catalogs above our S/N cut of 7. Therefore, the catalog completeness correction is very small and will not have a strong influence on the results presented in this section.

7.2. Point Source Completeness

To remove foreground galaxies from our quasar color selection, we only selected point sources by forcing a pGalaxy < 0.95 (Section 3). We tested the efficiency and completeness of this criterion in two different ways. First, we matched the VIKING data in the GAMA09 region with objects from the SDSS database (Data Release 8; Aihara et al. 2011). In a second test we used the VIDEO data to select a clean, photometric sample of stars in the region for which VIKING data exist.

In the GAMA09 region, there are 3653 objects that were classified as point sources in the SDSS imaging catalogs and had a spectroscopic classification “STAR.” In the same region, we selected 12618 objects that were classified as galaxies in both the imaging and spectroscopic SDSS data. Using our adopted point-source classifier, pGalaxy < 0.95 , we selected 3397 of the SDSS point sources and only 9 of the galaxies (0.07%). Based on these numbers, we estimate that our point-source completeness is 93.3%, and our sample has a purity of 99.7%.

To obtain a clean sample of stars in the VIDEO data, we selected objects for which the morphological information from the five VIDEO images (Z, Y, J, H, and K_s) indicate that

the source is stellar (i.e., the catalog parameter “mergedclass” set to -1 or -2). In addition, we required that the sources have optical–infrared colors close to the stellar locus (see, e.g., Figure 1 in Fleuren et al. 2012). This selection resulted in 2446 stellar sources in the VIDEO catalog that had a match in the VIKING data. In the VIKING catalogs 2287 of the 2446 point sources had $p\text{Galaxy} < 0.95$. This comparison implies that the VIKING catalogs have a point-source completeness of 93.5%.

We find that the fraction of point sources misclassified in the VIKING catalogs is small (6%–7%). Combined with the catalog completeness, we estimate that we are missing 10.7% of the point sources in our search.

7.3. Color Selection Completeness

To estimate which fraction of quasars we are missing due to our color criteria, we follow the approach by Willott et al. (2005) to clone SDSS spectra of lower redshift quasars and shift them to higher redshifts. An alternative method is to create artificial quasar spectra based on an empirical model for the spectral energy distribution (e.g., Fan 1999; McGreer et al. 2013). The main assumption of both methods is that the rest-frame UV spectral properties of quasars redward of the $\text{Ly}\alpha$ line do not evolve with redshift (e.g., Kuhn et al. 2001; Fan et al. 2004). Although the cloning of lower redshift quasar spectra could suffer from incompleteness due to the SDSS quasar selection function (e.g., Richards et al. 2002a; Worseck & Prochaska 2011), we decided to mimic the procedure of Willott et al. (2005) as our goal is to compare our results to the $z \sim 6$ quasar luminosity function presented in Willott et al. (2010b) that was derived using the same color completeness correction.

For the cloning we selected optical spectra of quasars from the fourth SDSS Quasar Catalog (Schneider et al. 2007). We needed to model colors of quasars in a redshift interval covering at least $6.4 < z < 7.5$ in the filters Z , Y , and J (Figure 2). Given the wavelength range of the SDSS spectra ($3800 \lesssim \lambda \lesssim 9200$), we chose to use SDSS quasars in the redshift range $3.4 < z < 3.5$ for the cloning. The SDSS archives the spectra of 428 quasars over this redshift interval; after culling for quality issues such as missing data and incorrect redshift estimates, this number is reduced to 405 spectra, which can be artificially redshifted. The absolute magnitudes of these quasars range from $M_{1450} = -24.8$ to $M_{1450} = -28.5$ with a median of $M_{1450} = -25.8$, close to the average of our newly discovered quasars.

The most significant difference between quasar spectra at $z \sim 3.5$ and $z \sim 6.5$ is the spectral energy distribution blueward of the $\text{Ly}\alpha$ transition due to absorption by neutral hydrogen. Broadly speaking, as the volume averaged HI content of universe increases toward higher redshifts, the absorption of photons in the line of sight redshifted to the wavelengths of $\text{Ly}\alpha$, $\text{Ly}\beta$, and higher order transitions becomes stronger. When cloning high redshift quasar spectra from a lower redshift sample this difference must be accounted for. We applied artificial absorption to the SDSS spectra at $3.4 < z < 3.5$ following the procedure of Willott et al. (2005). In short, Willott et al. (2005) corrected for $\text{Ly}\alpha$ absorption already present in the spectra of SDSS quasars using the IGM transmission as a function of redshift as measured by Songaila (2004). The transmission was sampled in large redshift intervals of $\Delta z = 0.1$, which acted to smooth out inhomogeneity of the IGM and reduce the difference between the average optical depth per pixel and the effective

optical depth. The spectra were then further corrected for $\text{Ly}\beta$ absorption where the $\text{Ly}\beta$ optical depth is given by $\tau_\beta = 0.4 \times \tau_\alpha$ (Fan et al. 2006). Higher order absorption is negligibly small and was therefore left uncorrected.

Once these corrections were applied to the low-redshift spectra, they were then artificially redshifted and artificial absorption was added blueward of $\text{Ly}\alpha$ and $\text{Ly}\beta$ according to the same relation from Songaila (2004). Complete absorption of the spectra was applied blueward of the Lyman limit (912 Å). The only difference between the procedure of Willott et al. (2005) and our procedure is that we have updated the transmission–redshift relation to reflect new measurements recently published by Becker et al. (2013) for redshifts up to $z \lesssim 5$. The transmission functions from Songaila (2004) and Becker et al. (2013) are in good agreement at $z \sim 5$, so we have not attempted to join the two functions.

Each of the artificial spectra was redshifted to $6.0 < z < 7.5$ in steps of $\Delta z = 0.01$ and multiplied by the transmission curves of the Z , Y , and J filters. The average fluxes in the filters were converted to observed magnitudes. To take photometric errors into account in the color completeness, we added random magnitude errors as a function of the S/N. Since each tile can have different relative depths between the Z , Y , and J images, we computed the color completeness for each tile. An example of the resulting color completeness as a function of redshift is shown in Figure 7. The completeness in other tiles looks very similar. At high S/N (i.e., negligible magnitude errors), the completeness for the conservative color criteria rises steeply between $z = 6.5$ and $z = 6.6$ and remains above $\sim 95\%$ up to $z = 7.2$. At higher redshifts the completeness drops quickly to 10% at $z = 7.5$. This is because at $z \gtrsim 7.1$ the IGM absorption cuts into the Y bandpass, and the model quasars move redder in $Y - J$. At $z \gtrsim 7.4$ the average $Y - J$ color of the model quasars is $Y - J > 0.5$, outside our selection region. At lower S/N the peak completeness drops to 75%–80% for artificial quasars with $(\text{S/N})_Y = 7$, while the redshift distribution broadens slightly. At the high redshift end, the completeness of the extended color criteria is identical to the one of the conservative color criteria. Due to the lower $Z - Y$ threshold in the extended color criteria, a higher fraction of artificial quasars at $6.4 < z < 6.6$ are selected.

Around a completeness of 30%–40%, the color completeness is almost independent of S/N. We therefore take the redshift range where the completeness is above 30% as the redshift range we probe with the VIKING data. For the conservative color criteria, the redshift range is $6.51 < z < 7.44$, and for the extended criteria it is $6.44 < z < 7.44$. The extended criteria are therefore sensitive for quasars down to the redshift where the highest redshift quasars are found in optical surveys (e.g., Willott et al. 2007). The surveyed area of 331.6 deg^2 and the probed redshift range of $\Delta z = 0.93$ ($\Delta z = 1.00$) for the conservative (extended) color criteria translates into a survey volume of $2.7 \text{ comoving Gpc}^3$ ($2.9 \text{ comoving Gpc}^3$).

To take the varying depth of the VIKING tiles (Figure 1) into account, we computed the color completeness for each tile as a function of absolute magnitude M_{1450} of the model quasars. In Figure 8 we show the completeness averaged over all tiles as a function of both redshift and absolute magnitude. The color completeness at $6.6 < z < 7.3$ drops to 50% (30%) for quasars with an absolute magnitude of $M_{1450} = -25.2$ (-25.07).

We will now apply all the completeness corrections to our data and compare the results with the expected number of quasars based on the extrapolated luminosity function of $z = 6$ quasars.

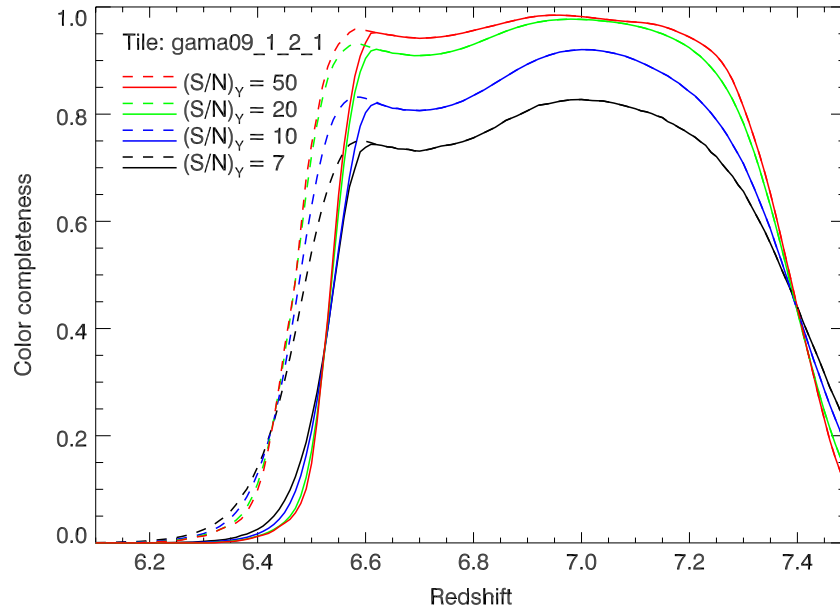


Figure 7. Color completeness as a function of redshift for tile gama09_1_2_1. The solid lines illustrate the completeness for the conservative color criteria, while the dashed lines represent the completeness when using the extended color criteria. The dashed lines overlap with the solid lines beyond $z \gtrsim 6.6$. From top to bottom the different lines demonstrate the change in completeness as a function of decreasing $(S/N)_Y$, going from $(S/N)_Y = 50$ to $(S/N)_Y = 7$. The extended color criteria is more sensitive for quasars in the range $6.5 \lesssim z \lesssim 6.6$ as compared to the conservative color criteria.

(A color version of this figure is available in the online journal.)

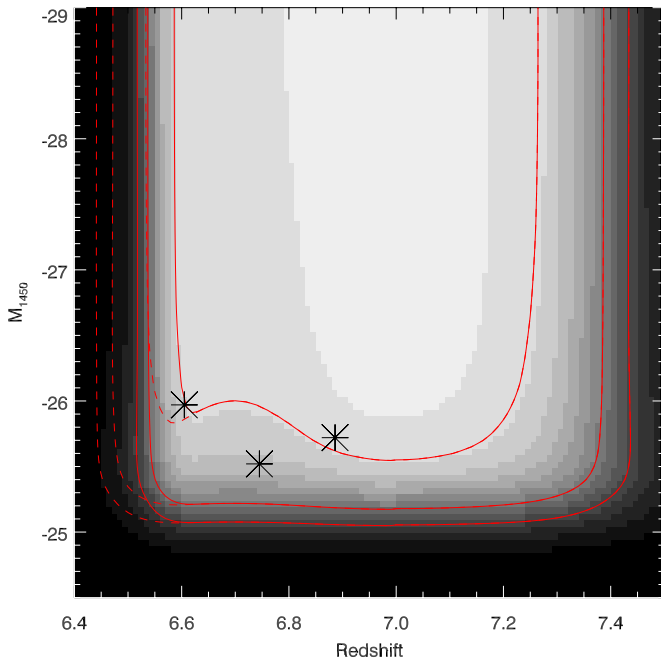


Figure 8. Color completeness averaged over all tiles as a function of redshift and M_{1450} . The colors illustrate the completeness with the conservative color criteria going from 98.8% (light gray) to 0% (black). The red, solid (dashed) contours show the 90%, 50%, and 30% completeness for the conservative (extended) color criteria. The large stars represent the redshift and absolute magnitude of our three new quasars. Our 50% color completeness reaches an absolute magnitude of -25.2 , and the 30% completeness reaches a slightly fainter absolute magnitude of -25.1 .

(A color version of this figure is available in the online journal.)

7.4. The Quasar Luminosity Function at $z \gtrsim 6.5$

The quasar luminosity function, $\Phi(M, z)$, is often parameterized by a double power-law (e.g., Boyle et al. 2000;

Fan et al. 2001):

$$\Phi(M, z) = \frac{10^{k(z-6)}\Phi(M^*, z=6)}{10^{0.4(\alpha+1)(M-M^*)} + 10^{0.4(\beta+1)(M-M^*)}}, \quad (1)$$

where α is the faint end slope, β the bright end slope, M the absolute magnitude, M^* the break magnitude, and $\Phi(M^*, z=6)$ the space density at $z=6$ of quasars with a magnitude M^* . The factor 10^{kz} accounts for the observed decline with redshift in the space density of quasars between $z=3$ and $z>5$ (e.g., Schmidt et al. 1995).

Willott et al. (2010b) compiled a sample of 40 quasars at $z \sim 6$ from various optical surveys to derive the $z \sim 6$ quasar luminosity function. Fixing the faint end slope to $\alpha = -1.5$, based on the quasar luminosity function at lower redshift (e.g., Croom et al. 2004), Willott et al. (2010b) determined the following best-fit parameters for the quasar luminosity function at $z=6$: $\Phi(M_{1450}^*) = 1.14 \times 10^{-8} \text{ Mpc}^{-3} \text{ mag}^{-1}$, $M_{1450}^* = -25.13$, and $\beta = -2.81$. A value of $k = -0.47$ was adopted by Willott et al. (2010b), which fits the evolution of the (bright end of the) luminosity function over the redshift range $3 < z < 6$ (Fan et al. 2001). Based on a study of $z \sim 5$ quasars, McGreer et al. (2013) derived a steeper decline in the space density of quasars with $M_{1450} < -25.5$ between $z \sim 4.9$ and $z=6$ of a factor 5.1 per unit redshift ($k = -0.71$).

If we assume that the quasar luminosity function evolves with constant parameters M_{1450}^* , β and α , and pure density evolution $\propto 10^{kz}$, then we can extrapolate the $z=6$ luminosity function to $z > 6.4$ and derive the expected number of high-redshift quasars in the VIKING survey. Assuming $k = -0.47$ we expect $0.0124 \text{ quasar deg}^{-2}$ down to $M_{1450} = -25.2$ in the redshift range $6.51 < z < 7.44$, while the extrapolated luminosity function predicts $0.0139 \text{ quasar deg}^{-2}$ in the redshift range $6.44 < z < 7.44$. In an area of 331.6 deg^2 we therefore expect on average ~ 4.1 quasars between $6.51 < z < 7.44$ and ~ 4.6 quasars at $6.44 < z < 7.44$ if we ignore any incompleteness.

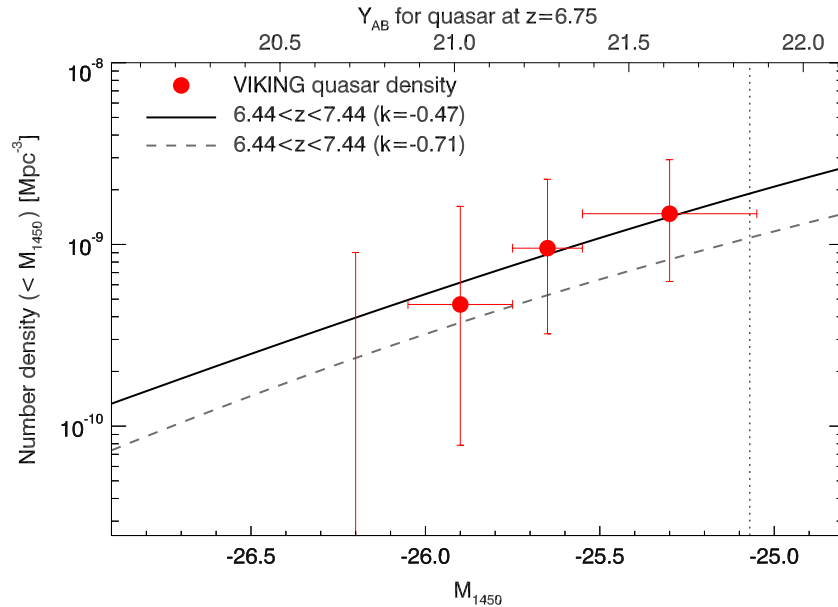


Figure 9. Cumulative quasar luminosity function at $z \sim 7$. The solid and dashed lines illustrate the predicted luminosity function in the redshift range $6.44 < z < 7.44$ based on the Willott et al. (2010b) $z = 6$ quasar luminosity function and a decline in number density with redshift $\propto 10^{-0.47z}$ and $\propto 10^{-0.71z}$, respectively. The number density of $6.44 < z < 7.44$ quasars implied by the new quasars has been computed in bins with a width of 0.1 mag. All bins brighter than the one centered on $M_{1450} = -26.0$ only have an upper limit to the number density. Bins having the same number density were grouped together in a single data point with a (horizontal) error bar. For models to predict (within 1σ) the same number of quasars as we observe, they should fall in the region that is outlined by the vertical error bars. The vertical dotted line denote the absolute magnitude above which our color completeness is $>30\%$.

(A color version of this figure is available in the online journal.)

The larger volume probed by the extended color criteria and the higher predicted space density of quasars at the lower end of our redshift range results in an increase of 13% in the expected number of quasars. With a sharper decline in the normalization of $k = -0.71$, the expected numbers are a factor of ~ 1.75 smaller.

In Figure 9 we show the cumulative luminosity function normalized over our surveyed volume and the completeness-corrected space density of $z \sim 7$ quasars derived from our newly discovered VIKING quasars. Although the follow up of all quasar candidates has not been completed, the observed density of $z > 6.44$ quasars is already fully consistent with the one predicted from the extrapolated $z = 6$ luminosity function. A steeper decline in space density at $z > 5$ as obtained by McGreer et al. (2013) underpredicts the density of quasars at $z \sim 7$ as found by our study. If we take the various sources of incompleteness into account, then with $k = -0.47$ we expect to find ~ 3.1 $z > 6.44$ quasars in our volume down to $M_{1450} = -25.2$. Assuming $k = -0.71$ we expect 1.8 quasars in the same volume. Therefore, given the large (Poisson) error on these estimates, we cannot rule out the steeper decline.

To estimate for which values of k we would expect to find three quasars in our survey volume, we extrapolated the $z = 6$ luminosity function to $6.44 < z < 7.44$ with k ranging from -3 to 0 in steps of 0.01 . For each value of k , we integrated the luminosity function down to $M_{1450} = -25.2$ and, including the various sources of incompleteness, computed the expected number of quasars in our probed volume. The best-fit value of k for which the expected number is three quasars and the 1σ confidence interval is $k = -0.49^{+0.28}_{-0.74}$. The best-fit value of $k = -0.49$ is close to the $k = -0.47$ Willott et al. (2010b) adopts. The best-fit value obtained by McGreer et al. (2013), $k = -0.71$, is nonetheless well within the range of k that fit our results.

8. SUMMARY AND DISCUSSION

We used the VIKING near-infrared imaging survey to search for quasars above a redshift $z \gtrsim 6.5$. We analyzed 332 deg^2 of VIKING data down to a median 7σ Y -band depth of 21.5. We employed two sets of color criteria to select potential quasars at high redshift. Our conservative color criteria is sensitive to quasars in the redshift range $6.51 < z < 7.44$, and with these criteria we selected 43 quasar candidates. Our extended color criteria probed an increased redshift range of $6.44 < z < 7.44$ and selected an additional 42 objects. After we obtained optical imaging of 45 quasar candidates with the NTT, 6 objects remained having colors consistent with high redshift quasars. Spectroscopic follow-up with VLT/FORS2 of four of these sources identified three previously unknown quasars with redshifts of $z = 6.6$ – 6.9 . The fourth object was a foreground star. The newly discovered quasars have the following characteristics.

1. The absolute magnitudes of the new quasars are in the range of $-25.5 < M_{1450} < -26.0$, which is about 1–2 mag fainter than the $z \sim 6$ quasars discovered in the SDSS main survey (Fan et al. 2006) and roughly similar to the quasars at $z \sim 6$ found in the deep stripe of the SDSS southern survey (Jiang et al. 2008). The only other $z \sim 7$ quasar published so far, J1120+0641 at $z = 7.1$, has an absolute magnitude of -26.6 (Mortlock et al. 2011), 0.6–1.1 mag brighter than the VIKING quasars presented in this article.
2. Near-infrared spectroscopy revealed that the new VIKING quasars exhibit emission lines commonly seen in lower redshift quasars, including Si IV $\lambda 1397 + \text{O IV}] \lambda 1402$, C IV $\lambda 1549$, C III] $\lambda 1909$, and Mg II $\lambda 2799$. Furthermore, J2348–3054 shows continuum absorption blueward of the C IV emission line and could be a BAL quasar.
3. Using the infrared spectra, De Rosa et al. (2013) determined the mass of the central black hole powering the quasars.

By fitting a Gaussian to the Mg II line and measuring the continuum luminosity, they estimate central black hole masses of $1\text{--}2 \times 10^9 M_{\odot}$. These black hole masses are very similar to those powering quasars at $z \sim 6$ that were discovered in the SDSS main survey (e.g., Jiang et al. 2007; Kurk et al. 2007; De Rosa et al. 2011), but generally more massive than those of the $z \sim 6$ quasars discovered in the CFHQS (Willott et al. 2010a). Ignoring any incompleteness in our quasar search we can set a lower limit to the density of supermassive black holes in the early universe. The discovery of three black holes with masses $\sim 1\text{--}2 \times 10^9 M_{\odot}$ in the 2.9 comoving Gpc³ probed in this study implies a minimum density of $\rho(M_{\text{BH}} > 10^9 M_{\odot}) > 1.1 \times 10^{-9} \text{ Mpc}^{-3}$.

To derive the space density of quasars in the volume probed by the VIKING data, we computed the efficiency of our selection criteria in order to correct for the incompletenesses in our quasar search. The volume density of quasars at $6.44 < z < 7.44$ that we derive agrees well with the extrapolated $z = 6$ quasar luminosity function. This includes a decline in the space density of quasars of a factor 3 per unit redshift, which was previously obtained by measuring the density of bright quasars between $3 < z < 6$. Our results do not support a steeper decline in the space density of quasars with redshift.

These findings imply that we should discover a significant number of quasars beyond $z \gtrsim 6.5$ in the remainder of the VIKING area. The total area that will be covered by VIKING will be 1500 deg². If we ignore any incompleteness, we expect 18–19 quasars between $6.51 < z < 7.44$ and ~ 21 quasars at $6.44 < z < 7.44$ in the VIKING area down to $M_{1450} < -25.2$. With a larger number of quasars we will be able to constrain the evolution of the quasar luminosity function at $z \sim 7$.

These new quasars are prime targets for various follow-up studies. In future articles we will study the emission lines that can be seen in the near-infrared spectra and examine the implications on the chemical enrichment near the black holes. The optical spectra will be used to derive constraints on the column density of neutral hydrogen along the line of sight. Furthermore, the Southern declination of the sources makes them ideal targets for ALMA observations to study the galaxies that host these quasars.

We thank the referee for valuable comments and suggestions. G.D.R. is grateful to the National Science Foundation for support of this work through grant AST-1008882 to The Ohio State University.

Funding for SDSS-III has been provided by the Alfred P. Sloan Foundation, the Participating Institutions, the National Science Foundation, and the U.S. Department of Energy Office of Science. The SDSS-III website is <http://www.sdss3.org/>.

SDSS-III is managed by the Astrophysical Research Consortium for the Participating Institutions of the SDSS-III Collaboration including the University of Arizona, the Brazilian Participation Group, Brookhaven National Laboratory, University of Cambridge, Carnegie Mellon University, University of Florida, the French Participation Group, the German Participation Group, Harvard University, the Instituto de Astrofísica de Canarias, the Michigan State/Notre Dame/JINA Participation Group, Johns Hopkins University, Lawrence Berkeley National Laboratory, Max Planck Institute for Astrophysics, Max Planck Institute for Extraterrestrial Physics, New Mexico State University, New York University, Ohio State University, Pennsylvania State University, University of Portsmouth, Princeton

University, the Spanish Participation Group, University of Tokyo, University of Utah, Vanderbilt University, University of Virginia, University of Washington, and Yale University.

Facilities: ESO:VISTA, NTT (EFOSC2), VLT:Antu (FOR22), VLT:Kueyen (X-Shooter), Magellan:Baade (FIRE)

REFERENCES

- Aihara, H., Allende Prieto, C., An, D., et al. 2011, *ApJS*, **193**, 29
 Appenzeller, I., Fricke, K., Fürtig, W., et al. 1998, *Msngr*, **94**, 1
 Arnaboldi, M., Neeser, M. J., Parker, L. C., et al. 2007, *Msngr*, **127**, 28
 Becker, G. D., Hewett, P. C., Worseck, G., & Prochaska, J. X. 2013, *MNRAS*, **430**, 2067
 Becker, G. D., Rauch, M., & Sargent, W. L. W. 2007, *ApJ*, **662**, 72
 Bolton, J. S., Haehnelt, M. G., Warren, S. J., et al. 2011, *MNRAS*, **416**, L70
 Bouwens, R. J., Illingworth, G. D., Oesch, P. A., et al. 2012, *ApJL*, **752**, L5
 Boyle, B. J., Shanks, T., Croom, S. M., et al. 2000, *MNRAS*, **317**, 1014
 Buzzoni, B., Delabre, B., Dekker, H., et al. 1984, *Msngr*, **38**, 9
 Croom, S. M., Smith, R. J., Boyle, B. J., et al. 2004, *MNRAS*, **349**, 1397
 Cushing, M. C., Vacca, W. D., & Rayner, J. T. 2004, *PASP*, **116**, 362
 Dalton, G. B., Caldwell, M., Ward, A. K., et al. 2006, *Proc. SPIE*, **6269**, 62690X
 De Rosa, G., Decarli, R., Walter, F., et al. 2011, *ApJ*, **739**, 56
 De Rosa, G., Venemans, B. P., Decarli, R., et al. 2013, *ApJ*, submitted (arXiv:1311.3260)
 Emerson, J., McPherson, A., & Sutherland, W. 2006, *Msngr*, **126**, 41
 Fan, X. 1999, *AJ*, **117**, 2528
 Fan, X., Hennawi, J. F., Richards, G. T., et al. 2004, *AJ*, **128**, 515
 Fan, X., Narayanan, V. K., Lupton, R. H., et al. 2001, *AJ*, **122**, 2833
 Fan, X., Strauss, M. A., Becker, R. H., et al. 2006, *AJ*, **132**, 117
 Findlay, J. R., Sutherland, W. J., Venemans, B. P., et al. 2012, *MNRAS*, **419**, 3354
 Fleuren, S., Sutherland, W., Dunne, L., et al. 2012, *MNRAS*, **423**, 2407
 Gnedin, N. Y., & Fan, X. 2006, *ApJ*, **648**, 1
 González-Solares, E. A., Walton, N. A., Greimel, R., et al. 2008, *MNRAS*, **388**, 89
 Grandi, S. A. 1982, *ApJ*, **255**, 25
 Gunn, J. E., & Stryker, L. L. 1983, *ApJS*, **52**, 121
 Hamuy, M., Suntzeff, N. B., Heathcote, S. R., et al. 1994, *PASP*, **106**, 566
 Hamuy, M., Walker, A. R., Suntzeff, N. B., et al. 1992, *PASP*, **104**, 533
 Hewett, P. C., Warren, S. J., Leggett, S. K., & Hodgkin, S. T. 2006, *MNRAS*, **367**, 454
 Irwin, M. J., Lewis, J., Hodgkin, S., et al. 2004, *Proc. SPIE*, **5493**, 411
 Jarvis, M. J., Bonfield, D. G., Bruce, V. A., et al. 2013, *MNRAS*, **428**, 1281
 Jiang, L., Fan, X., Annis, J., et al. 2008, *AJ*, **135**, 1057
 Jiang, L., Fan, X., Bian, F., et al. 2009, *AJ*, **138**, 305
 Jiang, L., Fan, X., Vestergaard, M., et al. 2007, *AJ*, **134**, 1150
 Kelson, D. D. 2003, *PASP*, **115**, 688
 Komatsu, E., Smith, K. M., Dunkley, J., et al. 2011, *ApJS*, **192**, 18
 Kuhn, O., Elvis, M., Bechtold, J., & Elston, R. 2011, *ApJS*, **136**, 225
 Kurk, J. D., Walter, F., Fan, X., et al. 2007, *ApJ*, **669**, 32
 Latif, M. A., Schleicher, D. R. G., Schmidt, W., & Niemeyer, J. 2013, *MNRAS*, **433**, 1607
 Lawrence, A., Warren, S. J., Almaini, O., et al. 2007, *MNRAS*, **379**, 1599
 Lewis, J. R., Irwin, M., & Bunclark, P. 2010, in *ASP Conf. Ser.* 434, *Astronomical Data Analysis Software and Systems XIX*, ed. Y. Mizumoto, K.-I. Morita, & M. Ohishi (San Francisco, CA: ASP), 91
 Lewis, J. R., Irwin, M. J., Hodgkin, S. T., et al. 2005, in *ASP Conf. Ser.* 347, *Astronomical Data Analysis Software and Systems XIV*, ed. P. Shopbell, M. Britton, & R. Ebert (San Francisco, CA: ASP), 599
 McGreer, I. D., Jiang, L., Fan, X., et al. 2013, *ApJ*, **768**, 105
 Modigliani, A., Goldoni, P., Royer, F., et al. 2010, *Proc. SPIE*, **7737**, 773728
 Morganson, E., De Rosa, G., Decarli, R., et al. 2012, *AJ*, **143**, 142
 Mortlock, D. J., Warren, S. J., Venemans, B. P., et al. 2011, *Natur*, **474**, 616
 Richards, G. T., Fan, X., Newberg, H. J., et al. 2002a, *AJ*, **123**, 2945
 Richards, G. T., Vanden Berk, D. E., Reichard, T. A., et al. 2002b, *AJ*, **124**, 1
 Schmidt, M., Schneider, D. P., & Gunn, J. E. 1995, *AJ*, **110**, 68
 Schneider, D. P., Hall, P. B., Richards, G. T., et al. 2007, *AJ*, **134**, 102
 Simcoe, R. A., Burgasser, A. J., Bernstein, R. A., et al. 2008, *Proc. SPIE*, **7014**, 70140U
 Simcoe, R. A., Burgasser, A. J., Bochanski, J. J., et al. 2010, *Proc. SPIE*, **7735**, 773514
 Simcoe, R. A., Sullivan, P. W., Cooksey, K. L., et al. 2012, *Natur*, **492**, 79

- Songaila, A. 2004, [AJ](#), **127**, 2598
- Vacca, W. D., Cushing, M. C., & Rayner, J. T. 2003, [PASP](#), **115**, 389
- Venemans, B. P., McMahon, R. G., Walter, F., et al. 2012, [ApJL](#), **751**, L25
- Venemans, B. P., McMahon, R. G., Warren, S. J., et al. 2007, [MNRAS](#), **376**, L76
- Vernet, J., Dekker, H., D'Odorico, S., et al. 2011, [A&A](#), **536**, A105
- Vernet, J., Kerber, F., Mainieri, V., et al. 2010, [HiA](#), **15**, 535
- Vestergaard, M., & Osmer, P. S. 2009, [ApJ](#), **699**, 800
- Vestergaard, M., & Wilkes, B. J. 2001, [ApJS](#), **134**, 1
- Walter, F., Riechers, D., Cox, P., et al. 2009, [Natur](#), **457**, 699
- Wang, R., Wagg, J., Carilli, C. L., et al. 2013, [ApJ](#), **773**, 44
- Willott, C. J., Albert, L., Arzoumanian, D., et al. 2010a, [AJ](#), **140**, 546
- Willott, C. J., Delfosse, X., Forveille, T., Delorme, P., & Gwyn, S. D. J. 2005, [ApJ](#), **633**, 630
- Willott, C. J., Delorme, P., Omont, A., et al. 2007, [AJ](#), **134**, 2435
- Willott, C. J., Delorme, P., Reylé, C., et al. 2010b, [AJ](#), **139**, 906
- Worseck, G., & Prochaska, J. X. 2011, [ApJ](#), **728**, 23